Catalytic oxidation of Li_2S on the surface of metal sulfides for Li–S batteries

Guangmin Zhou[a,1], Hongzhen Tian[b,1], Yang Jin[a,1], Xinyong Tao[a], Bofei Liu[a], Rufan Zhang[a], Zhi Wei Seh[c], Denys Zhuo[a], Yayuan Liu[a], Jie Sun[a], Jie Zhao[a], Chenxi Zu[a], David Sichen Wu[a], Qianfan Zhang[b,2], and Yi Cui[a,d,2]

[a]Department of Materials Science and Engineering, Stanford University, Stanford, CA 94305; [b]School of Materials Science and Engineering, Beihang University, Beijing 100191, People's Republic of China; [c]Institute of Materials Research and Engineering, Agency for Science, Technology and Research, Singapore 138634; and [d]Stanford Institute for Materials and Energy Sciences, Stanford Linear Accelerator Center National Accelerator Laboratory, Menlo Park, CA 94025

Edited by Thomas E. Mallouk, The Pennsylvania State University, University Park, PA, and approved December 6, 2016 (received for review September 22, 2016)

Polysulfide binding and trapping to prevent dissolution into the electrolyte by a variety of materials has been well studied in Li–S batteries. Here we discover that some of those materials can play an important role as an activation catalyst to facilitate oxidation of the discharge product, Li_2S, back to the charge product, sulfur. Combining theoretical calculations and experimental design, we select a series of metal sulfides as a model system to identify the key parameters in determining the energy barrier for Li_2S oxidation and polysulfide adsorption. We demonstrate that the Li_2S decomposition energy barrier is associated with the binding between isolated Li ions and the sulfur in sulfides; this is the main reason that sulfide materials can induce lower overpotential compared with commonly used carbon materials. Fundamental understanding of this reaction process is a crucial step toward rational design and screening of materials to achieve high reversible capacity and long cycle life in Li–S batteries.

lithium–sulfur batteries | catalytic oxidation | metal sulfides | graphene | polysulfide adsorption

The ever-increasing demand for energy storage devices with high energy density, low material cost, and long cycle life has driven the development of new battery systems beyond the currently dominant lithium ion batteries (LIBs) (1). Among alternative battery chemistries, lithium–sulfur (Li–S) batteries have attracted remarkable attention due to their high theoretical energy density of 2,600 watt hours per kilogram, 5 times higher than those of state-of-the-art LIBs (2–4). In addition, sulfur, as a byproduct of the petroleum refining process, is naturally abundant, inexpensive, and environmentally friendly (5). However, the practical application of Li–S batteries is still plagued with numerous challenges. For example, the insulating nature of sulfur and discharge products Li_2S/Li_2S_2 leads to low active material utilization. In addition, the easy dissolution of lithium polysulfides (LiPSs) into the electrolyte causes LiPSs shuttling between cathode and anode and uncontrollable deposition of sulfide species on the lithium metal anode, inducing fast capacity fading and low coulombic efficiency (2, 6).

Tremendous efforts have been taken to circumvent these concerns, with the nanostructuring of electrodes as one of the most effective approaches to overcoming the issues facing high-capacity electrode materials (2, 7). For example, the integration of nanostructured carbon materials with sulfur is one of the primary strategies for improving the electrical conductivity of the composites and suppression of polysulfide shuttling through physical confinement (8–14). However, it was first recognized by Zheng et al. (11) that the weak interaction between nonpolar carbon-based materials and polar $LiPSs/Li_2S$ species leads to weak confinement and easy detachment of LiPSs from the carbon surface, with further diffusion into the electrolyte causing capacity decay and poor rate performance. Therefore, the introduction of heteroatoms into carbonaceous materials (such as nitrogen, oxygen, boron, phosphorous, sulfur, or codoping) for the generation of polar functional groups was adopted to enhance the interaction and immobilization of LiPS species in the electrode (15). For instance, nitrogen- or sulfur-doped mesoporous carbons (16, 17), boron-doped carbons (18), oxygen- or nitrogen-functionalized carbon nanotubes and graphenes (19, 20), amino-functionalized reduced graphene oxides (21), and nitrogen/sulfur-codoped graphene sponges (22) have shown great promise in trapping LiPSs due to the strong anchoring sites induced by heteroatom doping. In addition to carbon, a wide variety of anchoring materials (AM) have been introduced with polysulfide binding and trapping abilities (23–25). Patterning of carbon- and tin-doped indium oxide for sulfur species deposition, as an example, offers a clear demonstration of the polysulfide binding effect (26). Various metal oxides (27, 28), metal sulfides (29–31), metal nitrides (32), metal carbides (33), and metal organic frameworks (34) have been proposed to overcome the above-mentioned problems and improve cycling stability based on their similar polar interaction with LiPSs or Lewis acid–base interaction.

Study in the past several years has indicated that polysulfide binding and trapping is one of the most important strategies for improving Li–S battery performance. Here we discover a catalytic effect: that electrode materials previously designed for polysulfide binding and trapping can play a critical role in catalyzing the oxidation of Li_2S back to sulfur during battery charging. The recent mechanism study has clarified that there are both

Significance

A series of metal sulfides were systematically investigated as polar hosts to reveal the key parameters correlated to the energy barriers and polysulfide adsorption capability in Li–S batteries. The investigation demonstrates that the catalyzing oxidation capability of metal sulfides is critical in reducing the energy barrier and contributing to the remarkably improved battery performance. Density functional theory simulation allows us to identify the mechanism for how binding energy and polysulfides trapping dominate the Li_2S decomposition process and overall battery performance. The understanding can serve as a general guiding principle for the rational design and screening of advanced materials for high-energy Li–S batteries.

Author contributions: G.Z., Y.J., Q.Z., and Y.C. designed research; G.Z., H.T., Y.J., and Q.Z. performed research; G.Z., H.T., Y.J., X.T., B.L., R.Z., Z.W.S., Y.L., J.S., J.Z., C.Z., D.S.W., Q.Z., and Y.C. contributed new reagents/analytic tools; G.Z., H.T., Y.J., X.T., B.L., R.Z., Z.W.S., D.Z., Y.L., J.S., J.Z., C.Z., D.S.W., Q.Z., and Y.C. analyzed data; and G.Z., D.Z., Q.Z., and Y.C. wrote the paper.

The authors declare no conflict of interest.

This article is a PNAS Direct Submission.

[1]G.Z., H.T., and Y.J. contributed equally to this work.

[2]To whom correspondence may be addressed. Email: yicui@stanford.edu or qianfan@buaa.edu.cn.

This article contains supporting information online at www.pnas.org/lookup/suppl/doi:10.1073/pnas.1615837114/-/DCSupplemental.

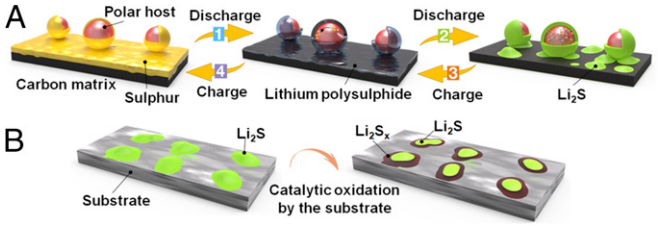

Fig. 1. Schematic illustration of the sulfur conversion process and the Li_2S catalytic oxidation on the surface of the substrate. (*A*) Sulfur adsorbs on the surface of carbon and polar host and transforms to Li_2S_x, which is strongly bonded with the polar host while weakly adsorbed by nonpolar carbon (step 1). Li_2S_x transforms to Li_2S and is mainly captured by the polar host while isolated islands are deposited on the carbon surface (step 2). (*B*) The substrate catalyzes Li_2S decomposition and favors the oxidization of Li_2S to Li_2S_x near the substrate surface, and finally to sulfur (steps 3 and 4 in *A*).

electrochemical and chemical pathways during battery cycling (35). That is, polysulfides can be electrochemically deposited to form Li_2S, or chemically disproportionated to form Li_2S, suggesting that the catalytic oxidation of Li_2S is of crucial importance in achieving high reversible capacity and long cycling life. Typically, the conversion reaction process in Li–S batteries can be divided into four main steps, as illustrated in Fig. 1. Most of the research work has emphasized the physical/chemical adsorption of sulfur species on the surface of carbon and polar hosts (strong affinity to LiPSs/Li_2S, step 1, Fig. 1*A*). For insulating materials with poor electronic conductivity, the polysulfide redox mechanism is hampered. Our group has recently demonstrated the importance of balancing sulfide species adsorption and diffusion on nonconductive metal oxides (27) with better surface diffusion, leading to higher Li_2S deposition efficiency (step 2, Fig. 1*A*). In the reverse reaction process, catalysis of the decomposition of Li_2S and oxidization of Li_2S to Li_2S_x and finally to sulfur (Fig. 1*B* and steps 3 and 4 in Fig. 1*A*) near the surface of the substrate are crucial steps to realizing high capacity and Columbic efficiency, yet have been relatively neglected in the Li–S chemistry. In this respect, a systematic consideration of the substrates that are capable of catalyzing Li_2S decomposition is critical to the development of advanced Li–S batteries.

Herein, a series of metal sulfides have been systematically investigated as model systems to identify the key parameters in determining the energy barrier for Li_2S oxidation and polysulfide adsorption capability in Li–S batteries. The experimental results show that VS_2-, TiS_2-, and CoS_2-based cathodes exhibit higher binding energy and lower diffusion and activation energy barriers, resulting in improved capacity and cycling stability. By combining first-principles calculations, we demonstrate that the strongly coupled interactions between LiPS species and metal sulfides and the energy barrier of Li_2S decomposition is correlated with the binding between isolated Li ions and the sulfur in sulfides. This strong interaction is favorable for lowering the overpotential and improving energy efficiency compared with weakly bonded carbon materials. These findings provide insight into a fundamental understanding of sulfur conversion chemistry and guidance for the future design and screening of new materials with Li_2S catalytic activity toward achieving high-performance Li–S batteries.

Results and Discussion

Initial Activation Energy Barrier on Various Metal Sulfides. To understand the role of metal sulfides in catalytic decomposition of Li_2S, we systematically investigated the effect of six kinds of metal sulfides, including VS_2, CoS_2, TiS_2, FeS, SnS_2, and Ni_2S_3, on tuning the decomposition energy barrier. According to our simulation of electronic band structures (*SI Appendix*, Fig. S1), Ni_3S_2, FeS, and CoS_2 are metallic materials and VS_2 and TiS_2 are semimetallic, which means that they are all materials with good electrical conductivities, whereas SnS_2 is a semiconductor with a band gap of 2.2 eV. Carbon materials [a graphene/carbon nanotube hybrid (G/CNT) (36) was used in this work] were chosen for comparison due to their common use as conductive coating materials in sulfur- or Li_2S-based cathodes. The cathode consists of a commercial Li_2S cathode material mixed uniformly with various metal sulfides, carbon black, and polyvinylidene fluoride binder. The detailed synthesis procedures are described in *SI Appendix*, *Materials and Methods*. Coin cells were assembled with lithium metal as anode and reference electrode. Li_2S suffers from a low electrical conductivity, high charge transfer resistance, and low lithium ion diffusivity, which leads to a high overpotential at the initial charging to overcome the energy barrier. The initial charge voltage profiles from open-circuit voltage to 4.0 V to delithiate Li_2S is shown in *SI Appendix*, Fig. S2. The red rectangular area was magnified in Fig. 2*A* to clearly show the activation barrier. The G/CNT–Li_2S cathode without the addition of metal sulfide exhibits a high potential barrier at about 3.41 V in the initial charging process, indicating a sluggish activation process with high charge transfer resistance. The SnS_2–Li_2S cathode shows a clear voltage jump with a potential barrier of 3.53 V during the activation process due to the semiconducting nature of SnS_2. The charge voltage plateaus after the short voltage jump represent the phase conversion reaction from Li_2S to low-order LiPSs, high-order LiPSs, and sulfur. A similar charging phenomenon is observed for Ni_3S_2–Li_2S and FeS–Li_2S electrodes with high potential barriers of 3.47 and 3.25 V even though both are metallic. However, the addition of CoS_2, VS_2, and TiS_2 significantly reduces the height of the potential barrier to 3.01, 2.91, and 2.88 V, respectively (Fig. 2*A*). These results are consistent with the cyclic voltammetry (CV) measurements (*SI Appendix*, Fig. S3). The lower potential barrier and longer voltage plateau of the CoS_2-, VS_2-, and TiS_2-based electrodes compared with other metal sulfides indicate improved conductivity and reduced charge transfer resistance.

To attain an in-depth understanding of the function of these metal sulfides, we use the climbing-image nudged elastic band

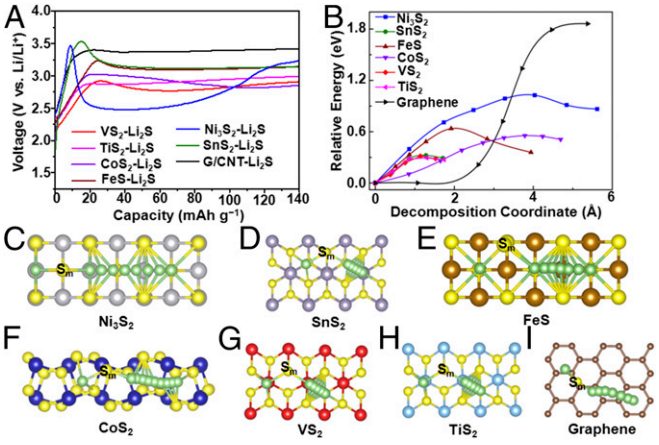

Fig. 2. Electrochemical activation and Li_2S decomposition mechanism on the surface of various metal sulfides and graphene. (*A*) First cycle charge voltage profiles of Ni_3S_2–Li_2S, SnS_2–Li_2S, FeS–Li_2S, CoS_2–Li_2S, VS_2–Li_2S, TiS_2–Li_2S, and G/CNT–Li_2S electrodes. (*B*) Energy profiles for the decomposition of Li_2S cluster on Ni_3S_2, SnS_2, FeS, CoS_2, VS_2, TiS_2, and graphene. Top view schematic representations of the corresponding decomposition pathways for (*C*) Ni_3S_2, (*D*) SnS_2, (*E*) FeS, (*F*) CoS_2, (*G*) VS_2, (*H*) TiS_2, and (*I*) graphene. Here, green, yellow, gray, purple, brown, blue, red, cyan, and beige balls symbolize lithium, sulfur, nickel, tin, iron, cobalt, vanadium, titanium, and carbon atoms, respectively. S_m represents the sulfur atom in the Li_2S cluster.

(CI-NEB) method (37) to calculate the barrier for Li_2S decomposition to evaluate the delithiation reaction kinetics on the surface of different metal sulfides. Here, we consider the decomposition process from an intact Li_2S molecule into an LiS cluster and a single Li ion ($Li_2S \rightarrow LiS + Li^+ + e^-$). The main evolution is composed of the Li ion moving far away from the S atom in the Li_2S molecule, which is accompanied by breaking of the Li–S bond. The energy profiles for the decomposition processes on different sulfides are shown in Fig. 2*B*, and the barrier heights are listed in *SI Appendix*, Table S1. The Ni_3S_2 decomposition barrier is as high as 1.03 eV, much larger than the other five cases, and is consistent with the large initial voltage barrier for Ni_3S_2-added Li_2S cathode. The barriers for FeS, CoS_2, VS_2, and TiS_2 are 0.63, 0.56, 0.31, and 0.30 eV, respectively, and qualitatively agree with the voltage magnitudes measured experimentally. For SnS_2, the calculated barrier for decomposition is as low as 0.32 eV, but experimentally exhibits a very large initial charge potential. This can be probably attributed to the insulating nature of SnS_2 and the electron–ion recombination process, which is the rate-determining step for the delithiation process, but not the Li decomposition process. Fig. 2 *C*–*H* illustrates the decomposition pathway for one Li ion departing from the LiS cluster on the surface of six kinds of sulfides. It can be clearly seen that the decomposition process is associated with the binding between the isolated Li ion and the sulfur in sulfides. This is the dominant reason that the sulfide anchor can induce a lower decomposition barrier compared with carbon materials. For graphene, the chemical interaction between the Li ion and carbon is much weaker, and, therefore, the decomposition process should have a very large activation energy barrier (Fig. 2*I*, 1.81 eV according to our simulation).

Interaction Between Polysulfides and Various Metal Sulfides. The discovery that Li_2S decomposition is related to Li ion binding with the host material propels us to understand the binding between metal sulfides and LiPSs. Therefore, polysulfide adsorption tests and X-ray photoelectron spectroscopy (XPS) studies were carried out to provide detailed information on the interaction between polysulfides and various metal sulfides. To probe the polysulfide adsorptivity, 0.005 M Li_2S_6 was prepared by chemically reacting sulfur with Li_2S in 1,3-dioxolane/1,2-dimethoxyethane solution (DOL/DME, 1:1 by volume). Different masses of metal sulfides and G/CNT with equivalent total surface area were added into the above solution for comparison. Unsurprisingly, after prolonged contact with Li_2S_6, nonpolar G/CNT has no observable effect on adsorbing polysulfides as the color of the solution remains the same as the control sample shown in Fig. 3*A*, indicating weak physical adsorption. FeS and SnS_2 demonstrate higher adsorption capability of Li_2S_6 compared with G/CNT, whereas Ni_3S_2 exhibits lower adsorption capability as demonstrated by the lack of any significant color change. In contrast, the originally yellow-colored polysulfide solution becomes colorless after the addition of TiS_2 or VS_2, and becomes much lighter in color for CoS_2, suggesting a strong interaction between Li_2S_6 and these sulfide hosts.

XPS analysis of the samples retrieved after the adsorption test provides additional evidence for the interaction between LiPSs and metal sulfides or G/CNT. Here we take VS_2, CoS_2, and G/CNT as examples. The V 2p spectra of VS_2 and VS_2–Li_2S_6 are shown in *SI Appendix*, Fig. S4*A*, in which two peaks located at 517.3 and 524.8 eV with an energy separation of 7.5 eV are attributed to the V $2p_{3/2}$ and V $2p_{1/2}$ spin-orbit levels of VS_2 (38). Upon contact with Li_2S_6, both peaks shift about 0.8 eV to 1.0 eV toward lower binding energy. The Li 1s spectrum of pristine Li_2S_6 exhibits an Li–S peak at around 56.3 eV (*SI Appendix*, Fig. S4*B*), which shifts to 56.1 eV after contact with VS_2. Both of the peak shifts in V 2p and Li 1s suggest the formation of chemical bonds between VS_2 and Li_2S_6. A similar shift trend was observed in the CoS_2–Li_2S_6 system (*SI Appendix*, Fig. S4 *C* and *D*). In contrast, almost no signal can be detected in the Li 1s spectrum of the G/CNT–Li_2S_6 sample, confirming the poor adsorption capability of nonpolar G/CNT with the polar Li_2S_6 molecule (*SI Appendix*, Fig. S5).

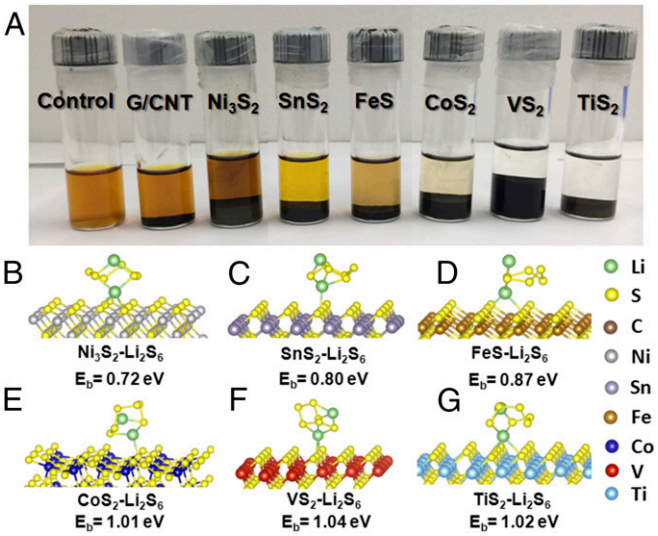

Fig. 3. Lithium polysulfide (Li_2S_6) adsorption by carbon and metal sulfides and corresponding simulation of Li_2S_6 adsorbed on the surface of metal sulfides. (*A*) Digital image of the Li_2S_6 (0.005 M) captured by carbon and metal sulfides in DOL/DME solution. Atomic conformations and binding energy for Li_2S_6 species adsorption on (*B*) Ni_3S_2, (*C*) SnS_2, (*D*) FeS, (*E*) CoS_2, (*F*) VS_2, and (*G*) TiS_2. Here, green, yellow, gray, purple, brown, blue, red, and cyan balls represent lithium, sulfur, nickel, tin, iron, cobalt, vanadium, and titanium atoms, respectively.

To study the interaction between Li_2S_6 and sulfide materials, first-principle simulations are applied. Fig. 3 *B*–*G* shows the adsorption conformations for Li_2S_6 on various sulfides. It can be clearly seen that the chemical interaction is dominated by the bond formed between the Li ion in Li_2S_6 and the sulfur ion in the sulfide, congruent with the previous discussion and the adsorption mechanism described in our previous work (39). The binding energy, E_b, is computed to measure the binding strength between the Li_2S_6 species and the AM; it is defined as the energy difference between the Li_2S_6–AM adsorbed system ($E_{Li2S6+AM}$) and the summation of pure Li_2S_6 (E_{Li2S6}) and pure AM (E_{AM}), which can be expressed as $E_b = E_{Li2S6} + E_{AM} - E_{Li2S6+AM}$ (positive binding energy indicates the binding interaction is favored and the larger the value, the stronger the anchoring effect). According to the simulation, the binding strengths between Li_2S_6 and Ni_3S_2, SnS_2, FeS, CoS_2, VS_2, and TiS_2 are 0.72, 0.80, 0.87, 1.01, 1.04, and 1.02 eV, respectively. The calculated magnitudes of E_b are in good agreement with our experimentally measured Li_2S_6 adsorption capability and also indicate that stronger interactions can induce a better anchoring effect. Furthermore, all of the sulfide anchors in our study can induce greater binding strength than graphene (0.67 eV), which exhibits weak chemical binding to Li_2S_6 as adsorption is dominated by physical van der Waals interaction (*SI Appendix*, Fig. S6); this explains why these sulfides can mitigate polysulfide dissolution and suppress shuttle effect, leading to better performance than commonly adopted sp^2 carbon materials in Li–S batteries.

Fabrication of Sulfur-Infiltrated Metal Sulfides@G/CNT Electrodes. To better disperse the metal sulfides (M_xS_y) in the sulfur cathode and reduce the weight of the whole cathode, a G/CNT hybrid was prepared and served as the substrate to support M_xS_y particles (*SI Appendix*, Fig. S7). The G/CNT and various commercial

M_xS_y particles were mixed, ground, and ball-milled for 1 h to disperse M_xS_y on the surface of the G/CNT and obtain M_xS_y@G/CNT hybrids (*SI Appendix*, Fig. S8). Sulfur was then infused through a melt diffusion method into the M_xS_y@G/CNT hybrids by heating at 155 °C for 12 h to form the S–M_xS_y@G/CNT composites. Here sulfur-infiltrated M_xS_y@G/CNT instead of Li_2S-based composites were used as cathodes because the cost of sulfur is much lower than that of Li_2S, and sulfur is easier to handle compared with Li_2S, as Li_2S is sensitive to water and oxygen. The intrinsically conductive M_xS_y in the electrode is intended to serve several important functions, including as a polar feature that can bind strongly to LiPSs, spatially localize the deposition of the sulfide species, and promote surface redox chemistry (*SI Appendix*, Fig. S8). The as-prepared M_xS_y@G/CNT composites were characterized by scanning electron microscopy (SEM) and transmission electron microscopy (TEM), as shown in *SI Appendix*, Fig. S9. These composites exhibit a cloud-like, rough surface with various M_xS_y particles well decorated inside or on the surface of the G/CNT (*SI Appendix*, Fig. S9 *A–F*). The microstructure was further investigated by TEM. The M_xS_y particles, with particle size in the range of 200 nm to 400 nm, are homogeneously distributed in the G/CNT hybrid without obvious agglomeration (*SI Appendix*, Fig. S9 *G–L*). It can be noted that the M_xS_y particles are firmly adhered to the G/CNT even after ultrasonic dispersion for TEM characterization, indicating good contact between them. The high-resolution TEM images show lattice spacings of 0.573, 0.568, 0.248, 0.298, 0.278, and 0.408 nm, which are ascribed to the (001), (001), (210), (110), (101), and (101) planes of VS_2, TiS_2, CoS_2, FeS, SnS_2, and Ni_3S_2, respectively (*SI Appendix*, Fig. S9 *M–R*). After the infusion of sulfur, the typical structure of the corresponding S–M_xS_y@G/CNT composites was characterized by SEM (energy-dispersive X-ray spectroscopy elemental analysis and mapping) and X-ray diffraction, as shown in *SI Appendix*, Figs. S10 and S11. The microstructure of the S–M_xS_y@G/CNT composite is similar to the M_xS_y@G/CNT composite in which the graphene and CNTs can still be sparsely observed. The surface of the S–M_xS_y@G/CNT composite is smoother after sulfur impregnation, suggesting a homogeneous sulfur coating on the surface of the M_xS_y@G/CNT hybrids.

Lithium Ion Diffusion Mechanism. The lithium ion diffusion coefficient can serve as a good descriptor to verify whether M_xS_y can propel the polysulfide redox reaction process, as fast lithium ion diffusion facilitates the sulfur transformation chemistry at the M_xS_y interface. CV was used to investigate electrode kinetics with respect to the lithium ion diffusion coefficient (27). Taking the S–VS_2@G/CNT electrode as a representative example, Fig. 4*A* shows the CV curves of the electrode measured under different scanning rates ranging from 0.2 $mV{\cdot}s^{-1}$ to 0.5 $mV{\cdot}s^{-1}$ between 1.5 V and 2.8 V (vs. Li/Li^+). At all scan rates, there are two cathodic peaks at around 2.30 V (I_{C1}) and 1.95 V (I_{C2}), corresponding to the reduction of elemental sulfur (S_8) to long-chain lithium polysulfides and the subsequent formation of short-chain Li_2S_2/Li_2S (12). The anodic peak at around 2.50 V in the anodic sweep results from the transition of Li_2S_2/Li_2S to polysulfides and elemental sulfur (I_A). The cathodic and anodic current peaks (I_{C1}, I_{C2}, I_A) of all of the M_xS_y-containing electrodes have a linear relationship with the square root of scanning rates (Fig. 4 *B–D*), indicative of the diffusion-limited process. Therefore, the classical Randles–Sevcik equation can be applied to describe the lithium diffusion process (27): $I_p = (2.69 \times 10^5)\, n^{1.5}\, S\, {D_{Li+}}^{0.5}\, C_{Li}\, \nu^{0.5}$, where I_P is the peak current, n is the charge transfer number, S is the geometric area of the active electrode, D_{Li+} is the lithium ion diffusion coefficient, C_{Li} is the concentration of lithium ions in the cathode, and ν is the potential scan rate. The slope of the curve ($I_p/\nu^{0.5}$) represents the lithium ion diffusion rate as n, S, and C_{Li} are unchanged. It can be clearly

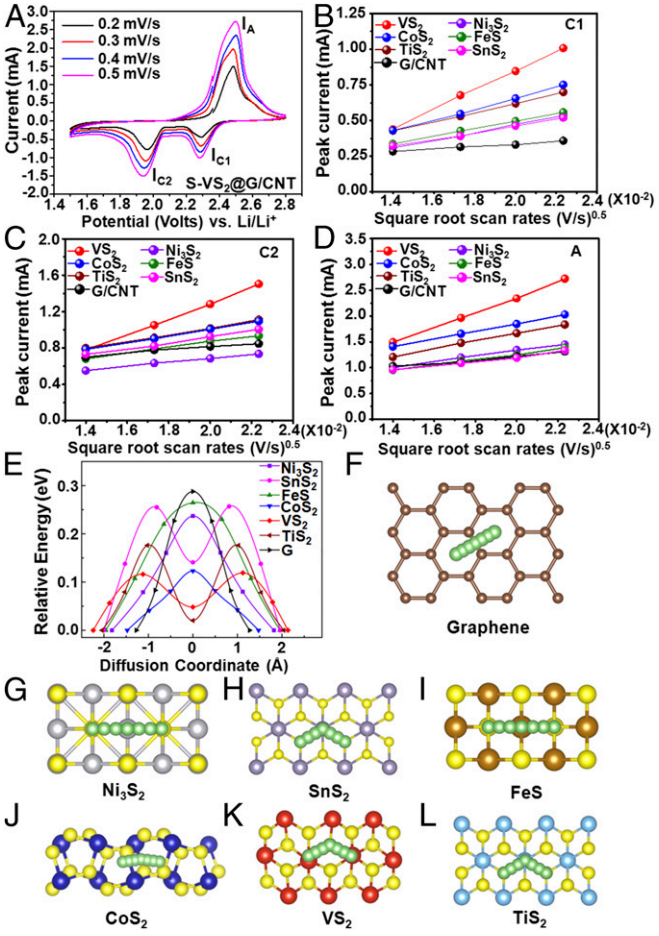

Fig. 4. Lithium ion diffusion properties on the surface of graphene and various metal sulfides with mechanism analysis. (*A*) CV curves of the S–VS_2@G/CNT electrode at various scan rates. Plots of CV peak current for the (*B*) first cathodic reduction process (I_{C1}: $S_8 \rightarrow Li_2S_x$), (*C*) second cathodic reduction process (I_{C2}: $Li_2S_x \rightarrow Li_2S_2/Li_2S$), and (*D*) anodic oxidation process (I_A: $Li_2S_2/Li_2S \rightarrow S_8$) versus the square root of the scan rates. (*E*) Energy profiles for diffusion processes of Li ion on Ni_3S_2, SnS_2, FeS, CoS_2, VS_2, TiS_2, and graphene. Top view schematic representations of corresponding diffusion pathways for (*F*) graphene, (*G*) Ni_3S_2, (*H*) SnS_2, (*I*) FeS, (*J*) CoS_2, (*K*) VS_2, and (*L*) TiS_2. Here, green, yellow, gray, purple, brown, blue, red, cyan, and beige balls represent lithium, sulfur, nickel, tin, iron, cobalt, vanadium, titanium, and carbon atoms, respectively.

seen that the S@G/CNT electrode exhibits the lowest lithium ion diffusivity, which mainly arises from the weak LiPSs adsorption and Li_2S catalyzing conversion capability, induced high LiPSs viscosity in the electrolyte, or deposition of a thick insulating layer on the electrode, as discussed previously. In contrast, the S–VS_2@G/CNT, S–CoS_2@G/CNT, and S–TiS_2@G/CNT electrodes demonstrate much faster diffusion compared with the S@G/CNT electrode and better reaction kinetics than the S–Ni_3S_2@G/CNT, S–SnS_2@G/CNT, and S–FeS@G/CNT electrodes, indicating that the introduction of polar M_xS_y hosts enables highly efficient catalyzing conversion of sulfur redox.

To validate the above-mentioned points, we simulate the diffusion barriers for Li ion on graphene and six kinds of sulfides using CI-NEB calculations (37). The energy profiles along the diffusion coordinate for these AM are shown in Fig. 4*E*. The magnitudes of the barriers lie in the region of 0.12 eV to 0.26 eV (listed in *SI Appendix*, Table S2), all of which are smaller than the diffusion barrier on graphene, which is 0.30 eV according to our simulations and is consistent with the experimental results

showing that Li ions diffuse faster on sulfide materials. The diffusion barriers for Ni_3S_2, SnS_2, and FeS are ~0.1 eV larger than those for CoS_2, VS_2, and TiS_2, which is also in qualitative agreement with our experimental observations. This finding likely explains why CoS_2, VS_2, and TiS_2 added electrodes have better reaction kinetics compared with the other three; a lower barrier can lead to an increase in the diffusion rate according to the exponential rule, and faster diffusion on the surface of the AM can promote the reaction between lithium and sulfur. In Fig. 4 *F*–*L*, the diffusion pathways on the surface of graphene and sulfides are illustrated. For Ni_3S_2, FeS, CoS_2, and graphene, the diffusion follows the arc curves from one stable point to the other, with the saddle point located in the middle of the pathway. In contrast, for hexagonal SnS_2, VS_2, and TiS_2, the diffusion follows a polyline, from one stable hollow site to the metastable hollow site and then to another stable hollow site. Therefore, the diffusions in these three kinds of sulfides have double-peak profiles.

Electrochemical Performance of the S–M_xS_y@G/CNT Electrodes. Fig. 5*A* and *SI Appendix*, Fig. S12 show the galvanostatic discharge/charge voltage profiles of S–M_xS_y@G/CNT and S@G/CNT electrodes at various current rates from 0.2 C (1 C = 1675 mA·g^{-1}) to 4 C in the potential range of 1.5 V to 2.8 V. The S–VS_2@G/CNT cathode exhibits excellent rate performance consisting of two discharge plateaus even at a very high current rate of 4 C (Fig. 5*A*), which can be ascribed to the reduction of S_8 to high-order lithium polysulfides at 2.3 V to 2.4 V and the transformation to low-order Li_2S_2/Li_2S at 1.9 V to 2.1 V (2). In the reverse reaction, two plateaus in the charge curve represent the backward reaction from lithium sulfides to polysulfides and finally to sulfur (12). These results are in good agreement with the reduction and oxidation processes established in the CV curves (Fig. 4*A*). Based on the discharge curves at 0.2 C, the sulfur electrodes containing G/CNT, SnS_2, Ni_3S_2, FeS, TiS_2, CoS_2, and VS_2 exhibit average discharge capacities of 685, 836, 845, 900, 1,008, 1,033, and 1,093 mA·h·g^{-1}, respectively (Fig. 5*B*). The higher discharge capacities of TiS_2-, CoS_2-, and VS_2-containing cathodes indicate the high utilization of sulfur due to the strong interaction between LiPSs and these sulfides. There are distinct differences in the voltage hysteresis and length of the voltage plateaus, which are related to the redox reaction kinetics and the reversibility of the system (Fig. 5*B* and *SI Appendix*, Fig. S12).

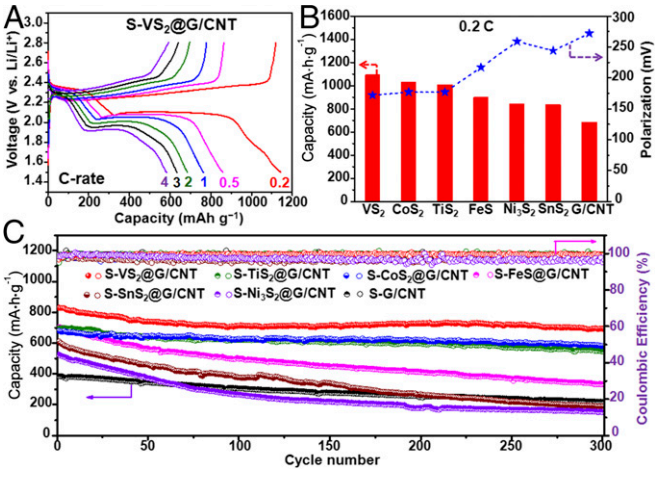

Fig. 5. Electrochemical performance of the S–M_xS_y@G/CNT composite electrodes. (*A*) Galvanostatic charge/discharge voltage profiles of the S–VS_2@G/CNT composite electrodes at different current densities within a potential window of 1.5 V to ~2.8 V vs. Li^+/Li^0. (*B*) Comparison of the specific capacity and polarization voltage between the charge and discharge plateaus at 0.2 C for different composite electrodes. (*C*) Cycling performance and coulombic efficiency of the different composite electrodes at 0.5 C for 300 cycles.

The TiS_2-, CoS_2-, and VS_2-containing cathodes display flat and stable plateaus with relatively small polarizations of 177, 177, and 172 mV at 0.2 C, much lower than G/CNT-, SnS_2-, Ni_3S_2-, and FeS-containing cathodes with values of 272, 244, 259, and 217 mV. This finding suggests a kinetically efficient reaction process with a smaller energy barrier promoted by the M_xS_y (TiS_2, CoS_2, and VS_2) catalyzing process discussed previously. A similar trend was confirmed when the cells were subjected to higher rates of 0.5 C and 1 C (*SI Appendix*, Figs. S12 and S13). The charge/discharge plateaus obviously shift or even disappear for G/CNT-, SnS_2-, and Ni_3S_2-containing electrodes at high current rates, indicating high polarization and slow redox reaction kinetics with inferior reversibility, which is consistent with the decomposition energy barrier analysis (Fig. 2).

Long-term cycling stability with high capacity retention is crucial for the practical application of Li–S batteries. Fig. 5*C* shows the cycling performance of the S@G/CNT and S–M_xS_y@G/CNT electrodes at 0.5 C for 300 cycles after the rate capability test. The S–VS_2@G/CNT electrode delivers a high initial reversible capacity of 830 mA·h·g^{-1}, and the capacity remains at 701 mA·h·g^{-1} after 300 cycles with stabilized coulombic efficiency above 99.5%, corresponding to a capacity retention of 84.5% and slow capacity decay rate of 0.052% per cycle. The high LiPSs adsorbing capability and good catalytic conversion of sulfur species alleviate the shuttle effect and improve the coulombic efficiency. The S–CoS_2@G/CNT and S–TiS_2@G/CNT electrodes also retain reversible capacities of 581 and 546 mA·h·g^{-1}, respectively, accounting for 85.3% and 78.2% of their initial capacities, with low capacity fading rates of 0.049% and 0.073% per cycle. Even at a high charge/discharge rate of 2 C, the VS_2-, CoS_2-, and TiS_2-based electrodes still demonstrate excellent cycling stability, with capacity retentions of 79.1%, 74.7%, and 73.7%, and low capacity decay rates of 0.070%, 0.084%, and 0.088% per cycle, respectively (*SI Appendix*, Fig. S14). The remarkable improvements in cycling stability and coulombic efficiency can be ascribed to the immobilization of soluble polysulfide species through a strong chemical binding and facile redox reaction propelled by these metal sulfides. As for the S@G/CNT electrode, it only delivers an initial reversible capacity of 386 mA·h·g^{-1} at 0.5 C rate and the capacity rapidly decreases to 218 mA·h·g^{-1} after 300 cycles, with a capacity retention of 56.5% and fast capacity decay rate of 0.145% per cycle. This finding suggests a weak affinity with LiPSs that cannot retard their diffusion into the electrolyte and prevent active material loss. Compared with TiS_2-, CoS_2-, and VS_2-containing electrodes, the sulfur cathodes containing FeS (334 mA·h·g^{-1}, 47.4% capacity retention), SnS_2 (191 mA·h·g^{-1}, 31.3% capacity retention), and Ni_3S_2 (153 mA·h·g^{-1}, 29.1% capacity retention) demonstrate inferior cycling stability at 0.5 C, with quick capacity degradation and unstable coulombic efficiency around 96%. The capacity fading rates reach 0.175%, 0.229%, and 0.236% per cycle for FeS-, SnS_2-, and Ni_3S_2-containing electrodes, respectively, much higher than the other three metal sulfides. These results imply that the selection of suitable polar hosts in the cathode that can (*i*) strongly interact with LiPSs, (*ii*) rationally control Li_2S deposition, (*iii*) enable fast lithium ion diffusion, (*iv*) effectively transform sulfur to LiPSs/Li_2S, and (*v*) catalytically reverse the reaction process is crucial and could significantly decrease polarization, improve sulfur utilization, and enhance rate performance and long-term cycling stability.

Postmortem Analysis of the Electrodes After Cycling. Postcycling SEM characterization provides additional evidence to demonstrate the strong chemisorption between M_xS_y and polysulfides in restricting LiPSs dissolution (*SI Appendix*, Figs. S15–S17). After 100 cycles, the morphologies of the S–M_xS_y@G/CNT electrodes display a relatively uniform and smooth surface with few aggregates observed on the surface (*SI Appendix*, Fig. S15). In contrast, large numbers of agglomerates covered the surfaces of the S@G/CNT electrode (*SI Appendix*, Fig. S16 *A* and *B*), indicating uncontrolled

diffusion of polysulfide intermediates that cause fast capacity decay during cycling. Some small cracks can be observed on the S–Ni_3S_2@G/CNT, S–SnS_2@G/CNT, and S–FeS@G/CNT electrodes (*SI Appendix*, Fig. S15 *A–C*), whereas the microstructures of the S–VS_2@G/CNT, S–CoS_2@G/CNT, and S–TiS_2@G/CNT electrodes (*SI Appendix*, Fig. S15 *D–F*) remained relatively unchanged, indicating their effective suppression of polysulfide shuttling. The microstructure evolution of lithium metal anode after cycling further supports the inhibition of the LiPSs shuttle effect and effective conversion of sulfur redox promoted by M_xS_y. A rough passivation layer with many cracks is observed on the Li anode surface of the S@G/CNT electrode due to the reaction of migrated sulfur species with the metallic lithium anode (*SI Appendix*, Fig. S16*C*), whereas the Li anode surface of S–M_xS_y@G/CNT electrodes is much smoother (*SI Appendix*, Fig. S17). Due to the strong chemical binding of CoS_2, VS_2, and TiS_2 to polysulfides (which significantly alleviates polysulfide shuttling) as well as the catalytic conversion of Li_2S/Li_2S_2 deposition, the passivation layers in the *SI Appendix*, Fig. S17 *D–F* are more intact and compact, elucidating the more stable cycling exhibited by S–CoS_2@G/CNT, S–VS_2@G/CNT, and S–TiS_2@G/CNT electrodes.

Conclusions

We have systematically investigated a series of metal sulfides as polar hosts to reveal the key parameters correlated to the energy barriers and polysulfide adsorption capability in Li–S batteries. Our results indicate that VS_2-, TiS_2-, and CoS_2-based cathodes exhibit higher capacity, lower overpotential, and better cycling stability compared with pure carbon materials and Ni_3S_2-, SnS_2-, and FeS-added electrodes. It is demonstrated that the inherent metallic conductivity, strong interaction with LiPSs, facilitated Li ion transport, controlled Li_2S precipitation, accelerated surface-mediated redox reaction, and catalyzing reduction/oxidation capability of M_xS_y are critical in reducing the energy barrier and contributing to the remarkably improved battery performance. More importantly, our density functional theory simulation results are in good agreement with our experiments measuring the activation barrier, polysulfide adsorption, lithium diffusion rate, and electrochemical behavior, which allows us to identify the mechanism for how binding energy and LiPSs trapping dominate the Li_2S decomposition process and overall battery performance. This understanding can serve as a general guiding principle for the rational design and screening of advanced materials for practical Li–S batteries with high energy density and long cycle life.

Materials and Methods

Materials and methods can be found in *SI Appendix*.

ACKNOWLEDGMENTS. Y.C. acknowledges support from the Assistant Secretary for Energy Efficiency and Renewable Energy, the Office of Vehicle Technologies, and the Battery Materials Research Program of the US Department of Energy. Q.Z. is supported by the National Natural Science Foundation of China (Grant 11404017), the Technology Foundation for Selected Overseas Chinese Scholar, the Ministry of Human Resources and Social Security of China, and the program for New Century Excellent Talents in University (Grant NCET-12-0033).

1. Bruce PG, Freunberger SA, Hardwick LJ, Tarascon J-M (2011) Li-O_2 and Li-S batteries with high energy storage. *Nat Mater* 11(1):19–29.
2. Yang Y, Zheng G, Cui Y (2013) Nanostructured sulfur cathodes. *Chem Soc Rev* 42(7): 3018–3032.
3. Manthiram A, Fu Y, Chung S-H, Zu C, Su Y-S (2014) Rechargeable lithium-sulfur batteries. *Chem Rev* 114(23):11751–11787.
4. Evers S, Nazar LF (2013) New approaches for high energy density lithium-sulfur battery cathodes. *Acc Chem Res* 46(5):1135–1143.
5. Chung WJ, et al. (2013) The use of elemental sulfur as an alternative feedstock for polymeric materials. *Nat Chem* 5(6):518–524.
6. Manthiram A, Chung S-H, Zu C (2015) Lithium-sulfur batteries: Progress and prospects. *Adv Mater* 27(12):1980–2006.
7. Sun Y, Liu N, Cui Y (2016) Promises and challenges of nanomaterials for lithium-based rechargeable batteries. *Nat Energy* 1:16071.
8. Wang D-W, et al. (2013) Carbon-sulfur composites for Li-S batteries: Status and prospects. *J Mater Chem A* 1(33):9382–9394.
9. Ji X, Lee KT, Nazar LF (2009) A highly ordered nanostructured carbon-sulphur cathode for lithium-sulphur batteries. *Nat Mater* 8(6):500–506.
10. Yang Y, et al. (2010) New nanostructured Li_2S/silicon rechargeable battery with high specific energy. *Nano Lett* 10(4):1486–1491.
11. Zheng G, et al. (2013) Amphiphilic surface modification of hollow carbon nanofibers for improved cycle life of lithium sulfur batteries. *Nano Lett* 13(3):1265–1270.
12. Zhou G, et al. (2013) Fibrous hybrid of graphene and sulfur nanocrystals for high-performance lithium-sulfur batteries. *ACS Nano* 7(6):5367–5375.
13. Jayaprakash N, Shen J, Moganty SS, Corona A, Archer LA (2011) Porous hollow carbon@sulfur composites for high-power lithium-sulfur batteries. *Angew Chem Int Ed Engl* 50(26):5904–5908.
14. Xin S, et al. (2012) Smaller sulfur molecules promise better lithium-sulfur batteries. *J Am Chem Soc* 134(45):18510–18513.
15. Zhang SS (2015) Heteroatom-doped carbons: Synthesis, chemistry and application in lithium/sulphur batteries. *Inorg Chem Front* 2(12):1059–1069.
16. Song J, et al. (2014) Nitrogen-doped mesoporous carbon promoted chemical adsorption of sulfur and fabrication of high-areal-capacity sulfur cathode with exceptional cycling stability for lithium-sulfur batteries. *Adv Funct Mater* 24(9):1243–1250.
17. See KA, et al. (2014) Sulfur-functionalized mesoporous carbons as sulfur hosts in Li-S batteries: Increasing the affinity of polysulfide intermediates to enhance performance. *ACS Appl Mater Interfaces* 6(14):10908–10916.
18. Yang C-P, et al. (2014) Insight into the effect of boron doping on sulfur/carbon cathode in lithium-sulfur batteries. *ACS Appl Mater Interfaces* 6(11):8789–8795.
19. Peng H-J, et al. (2014) Strongly coupled interfaces between a heterogeneous carbon host and a sulfur-containing guest for highly stable lithium-sulfur batteries: Mechanistic insight into capacity degradation. *Adv Mater Interfaces* 1(7):1400227.
20. Ji L, et al. (2011) Graphene oxide as a sulfur immobilizer in high performance lithium/sulfur cells. *J Am Chem Soc* 133(46):18522–18525.
21. Wang Z, et al. (2014) Enhancing lithium-sulphur battery performance by strongly binding the discharge products on amino-functionalized reduced graphene oxide. *Nat Commun* 5:5002.
22. Zhou G, Paek E, Hwang GS, Manthiram A (2015) Long-life Li/polysulphide batteries with high sulphur loading enabled by lightweight three-dimensional nitrogen/sulphur-codoped graphene sponge. *Nat Commun* 6:7760.
23. Wang JL, Yang J, Xie JY, Xu NX (2002) A novel conductive polymer-sulfur composite cathode material for rechargeable lithium batteries. *Adv Mater* 14(13-14):963–965.
24. Xiao L, et al. (2012) A soft approach to encapsulate sulfur: Polyaniline nanotubes for lithium-sulfur batteries with long cycle life. *Adv Mater* 24(9):1176–1181.
25. Chen H, et al. (2013) Ultrafine sulfur nanoparticles in conducting polymer shell as cathode materials for high performance lithium/sulfur batteries. *Sci Rep* 3:1910.
26. Yao H, et al. (2014) Improving lithium-sulphur batteries through spatial control of sulphur species deposition on a hybrid electrode surface. *Nat Commun* 5:3943.
27. Tao X, et al. (2016) Balancing surface adsorption and diffusion of lithium-polysulfides on nonconductive oxides for lithium-sulfur battery design. *Nat Commun* 7:11203.
28. Pang Q, Kundu D, Cuisinier M, Nazar LF (2014) Surface-enhanced redox chemistry of polysulphides on a metallic and polar host for lithium-sulphur batteries. *Nat Commun* 5:4759.
29. Seh ZW, et al. (2014) Two-dimensional layered transition metal disulphides for effective encapsulation of high-capacity lithium sulphide cathodes. *Nat Commun* 5:5017.
30. Pang Q, Kundu D, Nazar LF (2016) A graphene-like metallic cathode host for long-life and high-loading lithium-sulfur batteries. *Mater Horiz* 3(2):130–136.
31. Yuan Z, et al. (2016) Powering lithium-sulfur battery performance by propelling polysulfide redox at sulfiphilic hosts. *Nano Lett* 16(1):519–527.
32. Cui Z, Zu C, Zhou W, Manthiram A, Goodenough JB (2016) Mesoporous titanium nitride-enabled highly stable lithium-sulfur batteries. *Adv Mater* 28(32):6926–6931.
33. Liang X, Garsuch A, Nazar LF (2015) Sulfur cathodes based on conductive MXene nanosheets for high-performance lithium-sulfur batteries. *Angew Chem Int Ed Engl* 54(13):3907–3911.
34. Demir-Cakan R, et al. (2011) Cathode composites for Li-S batteries via the use of oxygenated porous architectures. *J Am Chem Soc* 133(40):16154–16160.
35. Xiao J, et al. (2015) Following the transient reactions in lithium-sulfur batteries using an in situ nuclear magnetic resonance technique. *Nano Lett* 15(5):3309–3316.
36. Zhao M-Q, et al. (2012) Graphene/single-walled carbon nanotube hybrids: One-step catalytic growth and applications for high-rate Li-S batteries. *ACS Nano* 6(12): 10759–10769.
37. Henkelman G, Uberuaga BP, Jonsson H (2000) A climbing image nudged elastic band method for finding saddle points and minimum energy paths. *J Chem Phys* 113(22): 9901–9904.
38. Rout CS, et al. (2013) Synthesis and characterization of patronite form of vanadium sulfide on graphitic layer. *J Am Chem Soc* 135(23):8720–8725.
39. Zhang Q, et al. (2015) Understanding the anchoring effect of two-dimensional layered materials for lithium-sulfur batteries. *Nano Lett* 15(6):3780–3786.